Nanoscale

PAPER

View Article Online
View Journal | View Issue

Check for updates

Cite this: Nanoscale, 2019, 11, 17111

A spin controlled wavefront shaping metasurface with low dispersion in visible frequencies†

Junxiao Zhou, ‡[a,b] Haoliang Qian,‡[b] Hailu Luo, *[a] Shuangchun Wen[a] and Zhaowei Liu*[b]

Received 26th April 2019,
Accepted 16th August 2019

DOI: 10.1039/c9nr03566d

rsc.li/nanoscale

Similar to amplitude and phase, optical spin plays an important and non-trivial role in optics, which has been widely demonstrated in wavefront engineering, creation of new optical components, and sensitive optical metrology. In this work, we propose and experimentally demonstrate a new type of spin controlled wavefront shaping metasurface. The proposed geometric phase metasurface is designed by employing the integrated and interleaved structures to independently control the left-handed and right-handed spin components. As an exemplary demonstration, our experimental results show that such a composite metasurface can convert a plane wave into a vortex beam and a Hermite beam for left-handed and right-handed polarized light, respectively. Because such a metasurface is made from non-resonant dielectric structures, it can work for broadband frequencies with very low dispersion. The proposed metasurface is fabricated by the laser writing method inside transparent glass with a low cost, which avoids the typical high-resolution lithography process. This spin dependent broadband wavefront shaping metasurface may find potential applications in optical communications, information processing, and optical metrology.

Introduction

The spin-based effects provide an effective route to manipulate the light field and its polarization state in micro/nanoscale photonics. In particular, the recent advances in the field of metasurfaces have significantly improved the capabilities to mold the flow of light beyond the traditional limits. A metasurface was originally developed for super-resolution focusing and imaging based on three-dimensional metamaterials,[1–3] and later adopted in two-dimensional cases for achieving ultrathin flat optical components.[4–8] They may achieve similar or sometimes better performance than the conventional optical elements and promote the creation of novel components with ultra-compact and more versatile functionalities. For instance, the metasurface can be designed for light focusing and imaging,[9–14] beam steering,[15–17] polarization conversion,[18–20] or enhanced photonic spin Hall effect.[21,22] A high-efficiency spin-independent controlled wavefront manipulation metasurface has been demonstrated at visible wavelengths based on the geometric phase, which is made of cylindrical nanopillars of the same height but of varying diameters depending on their radial position for controlling the local phase shift.[23] Compared with the spin insensitive method, a reflection geometry of the metasurface achieves a different hologram based on the geometric-phase approach, which is dependent on the incident spin.[24] Optical Spin as a degree of freedom is also proposed and employed for generating an arbitrary angular momentum.[25] Mueller *et al.* proposed that the combination of the propagation phase and the geometric phase can be utilized to control the arbitrary orthogonal states of polarization.[26] By designing a monolayer metasurface, it could simultaneously achieve circular asymmetric transmission and wavefront shaping based on asymmetric spin–orbit interactions.[27] Also, a recent study demonstrates a spin-controlled multifunctional shared-aperture array, which achieves the same left-handed and right-handed spin components with different topological charges.[28] Here in this work, we demonstrate that different wavefront shapings for left-handed and right-handed spin components can be achieved simultaneously by a single broadband geometric phase based dielectric metasurface. It could be regarded as a pseudo-symmetry broken spin-splitting instead of the symmetric case performed in our previous work.[14] Our design could work with both linearly and circularly polarized incident light at the transmitted mode, which is easier to be integrated and is more compact compared with the reflected mode.[24] Our metasurface is made by the laser writing method inside glass, opening up new opportunities for easy integration

[a] *Key Laboratory for Micro-/Nano-Optoelectronic Devices of Ministry of Education, School of Physics and Electronics, Hunan University, Changsha 410082, China. E-mail: hailuluo@hnu.edu.cn*

[b] *Department of Electrical and Computer Engineering, University of California, San Diego, 9500 Gilman Drive, La Jolla, California 92093, USA. E-mail: zhaowei@ucsd.edu*

† Electronic supplementary information (ESI) available. See DOI: 10.1039/c9nr03566d

‡ These authors contributed equally to this work.

with the existing optical components. Based on our design, different types of spin component, as an additional degree of freedom, will provide new opportunities for potential applications in optical communications and optical metrology.

To illustrate the basic working principles, we show the procedures of designing such a metasurface, which converts an incident plane wave into a vortex beam or a Hermite beam depending on the helicity of the incident beam. Fig. 1 schematically shows the expected function of the spin dependent wavefront shaping metasurface. When a linearly polarized plane wave is normally incident on the metasurface, it splits into different chiral components in opposite directions. In addition, the left-handed and right-handed components will be transformed into a vortex beam and a Hermite beam, respectively. These functions are enabled by the interleaved nanostructure with a special design, shown in red and blue structures in the metasurface. Furthermore, four spin components with different wavefronts and foci are demonstrated, which indicates that our concept can be employed to control and achieve arbitrary wavefront shaping. All these spin dependent functionalities are attained over a broadband wavelength range from visible to near infrared. The concept of this work can also be extended to generate beams with multichannel orbital angular momentum (OAM), which may find useful applications in integrated optics and optical communications.[29]

Design

To obtain a spin-dependent splitting, a metasurface comprising an array of anisotropic elements is used to obtain different phase gradients in response to LCP (left-handed circularly polarized) and RCP (right-handed circularly polarized) beams, so that these circularly polarized components are transmitted in different directions. This technique has been proposed by continuously controlling the local orientation and period of a subwavelength grating to achieve a geometric phase.[30] When an incident plane wave with an arbitrary polarization state is incident on the metasurface, the output field can be expressed as $|E_{\text{out}}\rangle = \eta_{\text{E}}|E_{\text{in}}\rangle + \eta_{\text{R}}e^{i2\theta}|R\rangle + \eta_{\text{L}}e^{-i2\theta}|L\rangle$. Here, $\eta_{\text{E}} = (t_x + t_y e^{i\phi})/2$, $\eta_{\text{R}} = (t_x - t_y e^{i\phi})\langle E_{\text{in}}|L\rangle/2$, and $\eta_{\text{L}} = (t_x - t_y e^{i\phi})\langle E_{\text{in}}|R\rangle/2$ represent the coupling efficiency for different polarization orders, and ϕ is the phase retardation or phase delay of the designed metasurface, which is equal to π in this work. $\langle E_{\text{in}}|R,L\rangle$ is an inner product with $|R\rangle = (1,0)^T$ and $|L\rangle = (0,1)^T$ as the right-handed and left-handed circular polarization components, respectively. From the output field equation, we can see that the emerging beam consists of three polarization orders. The first item retains the original polarization state and phase of the incident beam. The second and third items are right-handed and left-handed circular polarization components, which experience an inverse phase modification of $2\theta(x,y)$ and $-2\theta(x,y)$,[31,32] respectively, assuming that θ is the slow axis orientation of the element.

The design principle of the metasurface is schematically shown in Fig. 2. By employing the integrated and interleaved concept, the phase distribution of the vortex metasurface and the Hermite metasurface, and the integrated and interleaved metasurface is illustrated in Fig. 2(a), (d) and (g). For achieving the result of spin controlled wavefront shaping as shown in Fig. 2(c), (f) and (i), we designed the slow axis orientation

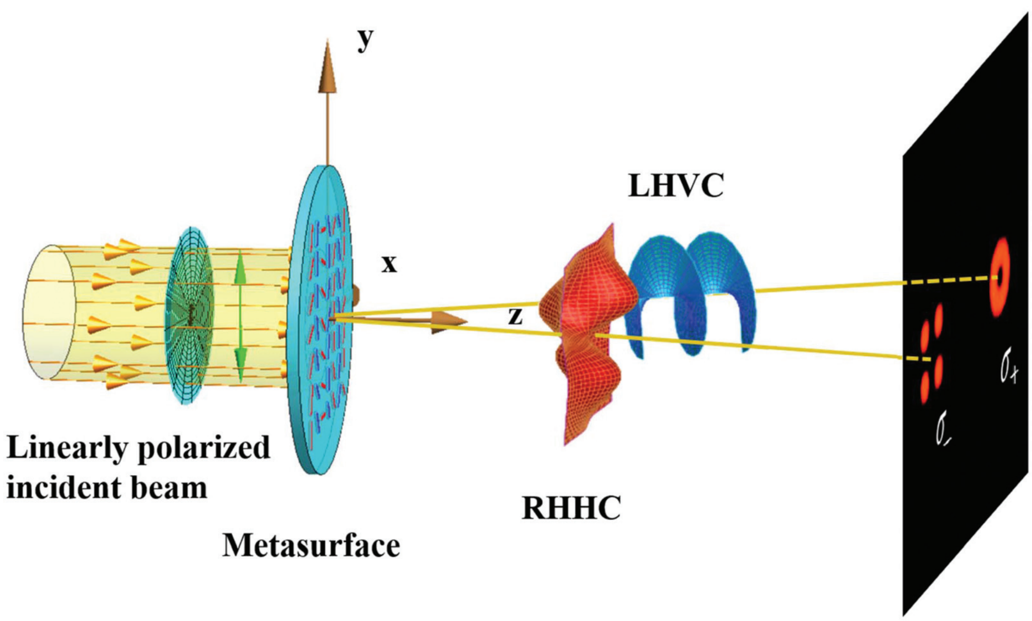

Fig. 1 Schematic illustration of the free space spin controlled wavefront shaping based on a single dielectric geometric phase metasurface. The green arrow indicates that the incident beam is linearly polarized. LHVC, left-handed vortex component. RHHC, right-handed Hermite component. The symbols σ_+ and σ_- represent the polarization helicity of spin components.

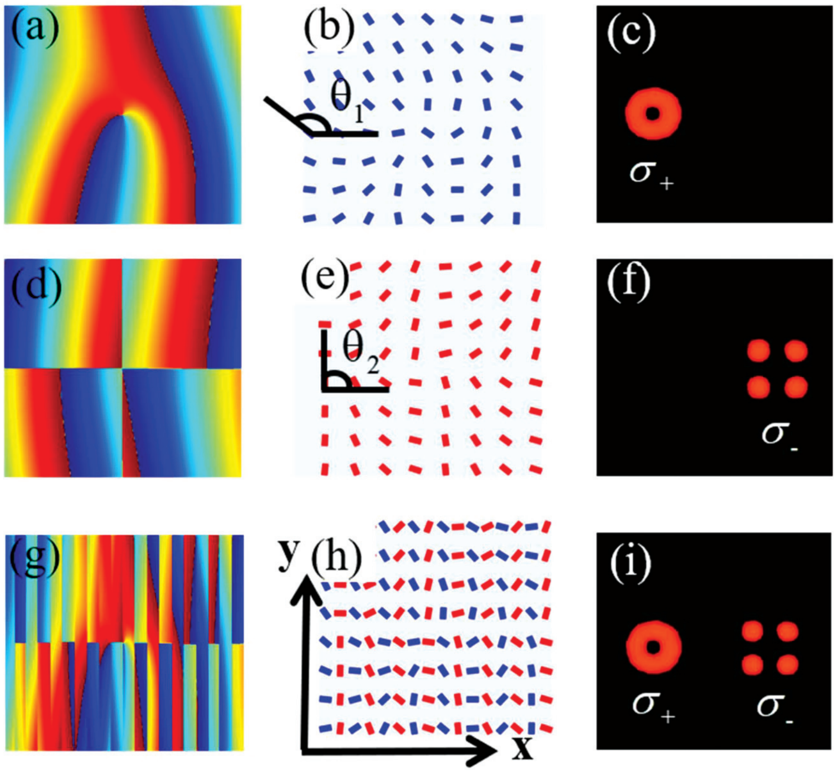

Fig. 2 The design principle for the metasurface and calculated results of the spin controlled wavefront shaping. (a)–(c) The designed phase distribution, slow axis orientation and the calculated far-field intensities for a linearly polarized incident beam incident on the vortex metasurface. (d)–(f) The illustration is the same as those of the first row, but for the case of generating the right-handed Hermite component. (g)–(i) The case of the interlevel concept for generating different wavefronts.

of the device based on the desired geometric phase. The axis orientation θ_1 obtained based on the phase distribution of a vortex metasurface in Fig. 2(a) is schematically represented in Fig. 2(b), which can be expressed as $\theta_1 = l \times \mathrm{Arg}(\mathrm{v}) + \frac{2\pi}{\lambda}\frac{x}{\Lambda} - \frac{2\pi}{\lambda}\sqrt{x^2+y^2}$. Here, Arg(v) is the phase of the vortex mode and l is the topological charge of the vortex component and is equal to 1 in this current design. Λ = 0.4 mm is the period of the polarization grating with the geometric phase induced by varying the axis orientation in the x direction. The combination of the first two terms is employed to generate the two mirror-symmetry spin components. The last term is used to generate the radial phase gradient for allowing the left-handed vortex component to converge and the right-handed spin component to diverge. In analogy to the vortex mode metasurface discussed above, a Hermite metasurface can be designed in a similar way. The axis orientation as shown in Fig. 2(e) is given as $\theta_2 = \mathrm{Arg}(\mathrm{u}) + \frac{2\pi}{\lambda}\frac{x}{\Lambda} + \frac{2\pi}{\lambda}\sqrt{x^2+y^2}$, where Arg(u) is the phase distribution of the Hermite (1,1) mode as an example.[33] Using the interleaved concept, we combine the Hermite mode metasurface and the vortex mode metasurface to obtain the final metasurface axis orientation shown in Fig. 2(h).

Experimental section

As shown in Fig. 3(a), the sample is made of form-birefringent nanostructured glass slabs,[34] which is based on a similar principle to that of the liquid q-plate, but overcoming the low resolution and damage threshold.[35] The glass substrate has a diameter of 2.5 cm with a thickness of 3 mm, and the metasurface area of this sample is 0.6 × 0.6 mm. The fabrication method is similar to what we have described in the previous work.[14] In this study, we had two interleaved nanostructure patterns. The written sample is irradiated with a mode-lock regenerative amplified Yb:KGW (ytterbium-doped potassium gadolinium tungstate) based femtosecond laser system (Pharos, Light Conversion Ltd) working at a 1030 nm wavelength (photon energy ~1.2 eV) and the repetition rate is about 500 kHz. The laser beam is focused at 250 μm below the sample (silica) surface *via* a 0.16 numerical aperture spherical lens. The polarization of the incident beam is controlled by an achromatic half-wave plate which is mounted onto a motorized rotation stage. The sample is mounted onto a three-axial air-bearing translation stage system (Aerotech Ltd) and is moved along the trajectory based on our design by controlling the stage using SCA software (Altechna Ltd). Under intense laser irradiation, a high free electron density is generated by multi-

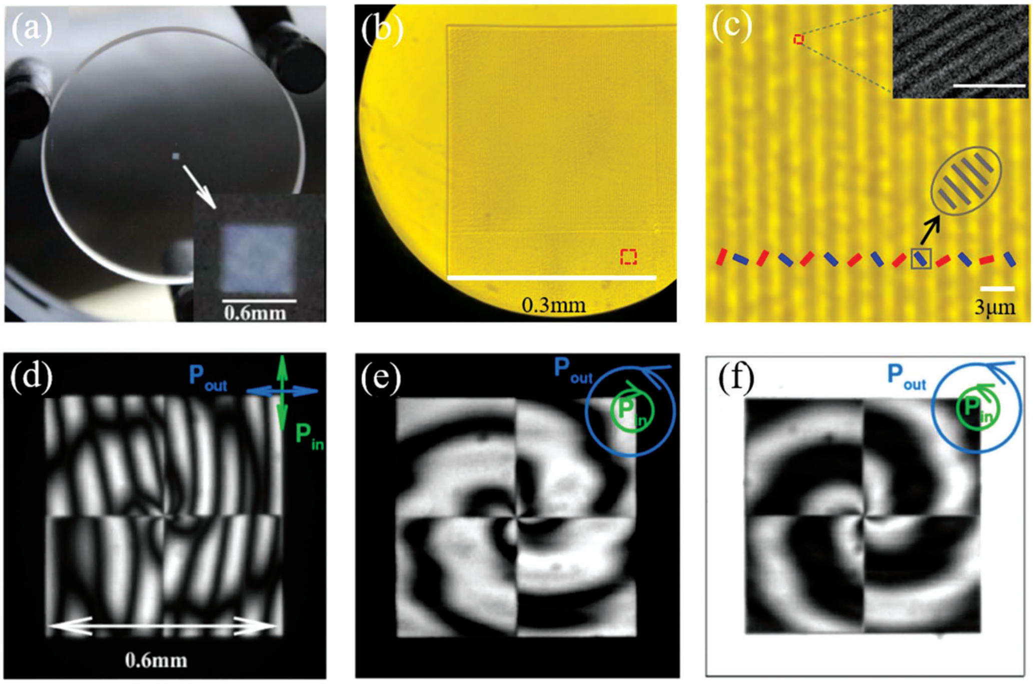

Fig. 3 The characterization of the integrated spin dependent wavefront shipping metasurface. (a) A photograph of the metasurface fabricated inside silica glass. The inset image shows the zoomed-in view of the center metasurface area. (b) Optical microscopy image of the upper-left corner of the sample pattern. (c) Enlarged microscopy image of the red dotted box in (b). Interleaved written nanostructure located on the sample's dark regions. Inset: scanning electron microscopy image. Scale bar, 300 nm. (d) Polariscopic analysis carried out by optical imaging between crossed linear polarizers. (e) Crossed circular polarizer imaging (f) and parallel circular polarizer imaging. P_{in} and P_{out} denote the input and output polarization states of light.

photon ionization under intense laser irradiation, creating plasma properties of the fused glass. Afterward, the plasma wave interferes with the incident light beam, forming a stripe-like nano-grating or a nanostructure.[36] The stripes are aligned perpendicular to the laser polarization direction. By changing the laser polarization gradually, the nanostructure with gradually varying orientation will be achieved. The self-organized nanostructure can be treated as a form-birefringent material with fast and slow axes oriented parallel and perpendicular to the stripes, respectively. The sample's refractive index can be modulated with the laser irradiation intensity and leads to the formation of birefringence in the isotropic glass sample where the uniform glass sample (SiO_2) decomposes into porous glass (SiO_{2-x}). The effective ordinary and extraordinary refractive indices are as follows: $n_o = \sqrt{f \times {n_1}^2 + (1-f) \times {n_2}^2}$, $n_e = \sqrt{{n_1}^2 \times {n_2}^2 / [f \times {n_1}^2 + (1-f) \times {n_2}^2}$. Here, f is the filling factor and n_1 and n_2 are the refractive indices of the two media which form the nanostructure. Thus, the phase retardation $\vartheta = 2\pi(n_e - n_o)h/\lambda$, which can be determined by the fill factor and writing depth. By choosing a certain fill factor f and thickness h, it can satisfy the desired phase retardation criteria, which is similar to the conventional birefringent crystals. In this work, we choose the phase retardation ϑ equal to π at the wavelength of 633 nm, the filling factor $f \approx 0.15$, and the writing period around 280 nm. So the value of $n_e - n_o$ can be obtained approximately as $-(2\text{–}4) \times 10^{-3}$ and the written depth h can be determined to be ~100 μm, respectively.

To demonstrate the local optical axis orientation and the phase retardation property of this sample, the polariscopic optical characterization of the sample is implemented in this work.[37] Fig. 3(b) shows the optical microscopy image of the upper-left corner of the pattern. Fig. 3(c) shows the zoomed-in view of the red dotted box in Fig. 3(b). The dark lines represent the laser written regions. The width of the dark lines is around 1 μm (see Fig. 3(c)), which is mainly determined by the focal size of the pulsed laser. The self-organized nanostructure typically has a period order of 300 nm. The color-coded bars (red and blue for LCP and RCP, respectively) in Fig. 3(c) indicate the orientation of the nanostructure. More details of the sample information can be found in ref. 14 and 30. Fig. 3(d)–(f) show the imaging results of the crossed linear, crossed circular, and parallel circular polarizers. The polariscopic characterization is in accordance with our design. The spiral shape in their center indicates the modulated vortex component corresponding to the vortex phase shown in Fig. 2(a). It can also be seen that the sample is composed of four regimes, which is led by the Hermite phase pattern shown in Fig. 2(d). From Fig. 3(e) and (f), it can be found that this sample possesses the opposite response of the left-handed and right-handed incident beams. The dark areas in Fig. 3(e) are bright in Fig. 3(f), and *vice versa*, which corresponds to the spin-dependent property of our sample.

An experiment setup built to validate the spin-dependent splitting generated by our sample is shown in Fig. 4(a). The fundamental Gaussian beam comes from a supercontinuum laser (SuperK EXW-12, NKT Photonics). The variable optical attenuator (VOA) is used to adjust the intensity of the laser beam. The beam's polarization state is controlled by the combination of a linear polarizer followed by a quarter-wave plate. A Glan laser polarizer (GLP) with an angle of 45° to a quarter-wave plate is used to generate a left-handed circular polarization of the incident light. By tuning the wavelength of the laser from 633 nm, 510 nm, and 480 nm, to 430 nm, the experimental results are recorded on a charge coupled device (CCD) as shown in Fig. 4(b)–(e). For the results of the next row, we set the GLP with an angle of 135° to obtain the RCP beam. When the quarter-wave plate is removed, the results of the linearly polarized incident beam are shown in the last row. All these results are in accordance with our theoretical calculations, as described in Fig. 2. In addition, it also demonstrates the broadband property of our composite metasurface with very small dispersion.

Based on the introduced integrated and interleaved metasurface concept, we also investigated the spin-dependent wavefront shaping with more complex spin-dependent component types and arbitrary spin-dependent shifts. We illustrate it by the example of the spin splitting of four different types: Gaussian, vortex, Airy and Hermite modes, as numerically shown in Fig. 5.

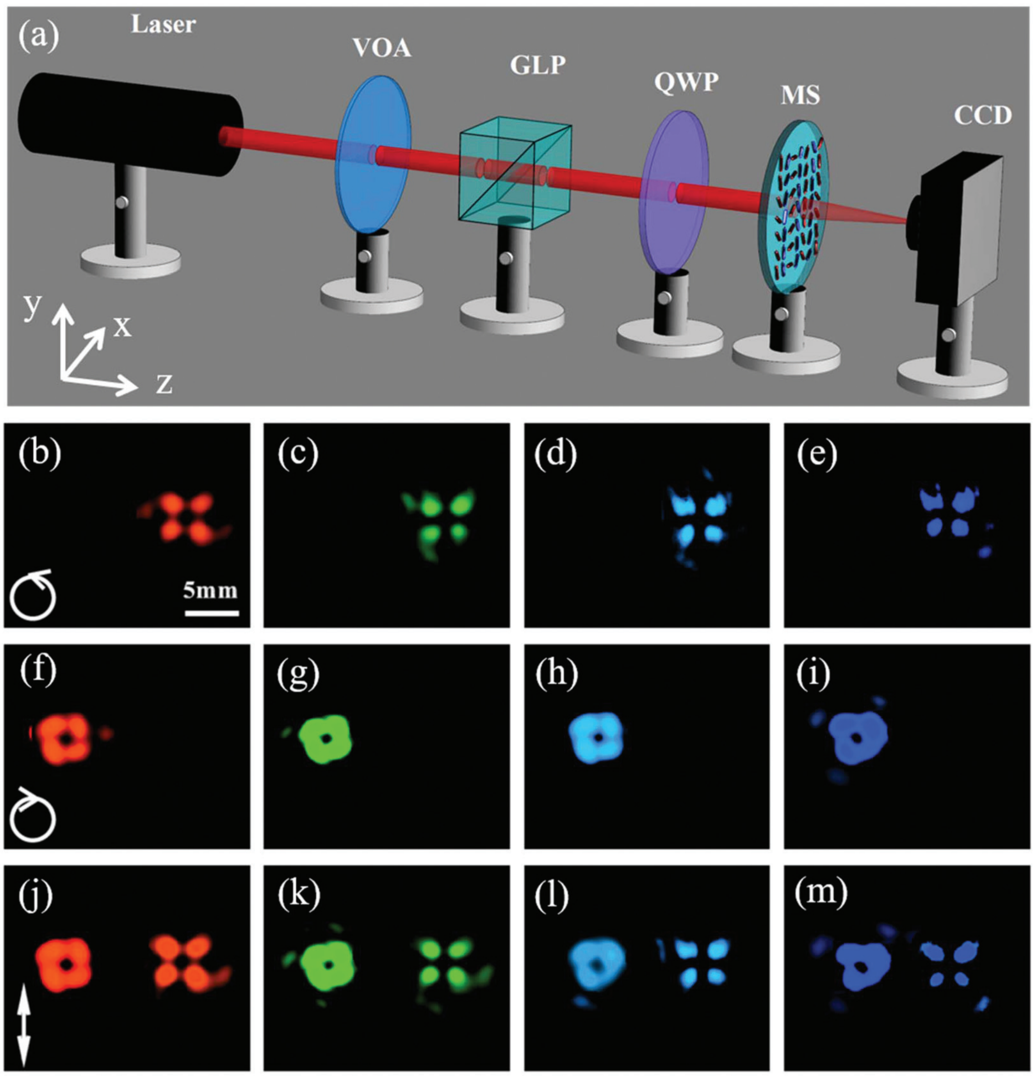

Fig. 4 Experimental demonstration of the spin dependent wavefront shaping metasurface in visible frequencies. (a) Experimental setup. VOA, variable optical attenuator; GLP, Glan laser polarizer; QWP, quarter-wave plate; MS, metasurface; CCD, charge coupled device. (b)–(m) Experimentally measured intensity distribution at a wavelength of 633 nm, 510 nm, 480 nm, and 430 nm from the left to right. (b)–(e), (f)–(i), and (j)–(m) are the results of the left-handed, right-handed circularly and linearly polarized incident beam, respectively.

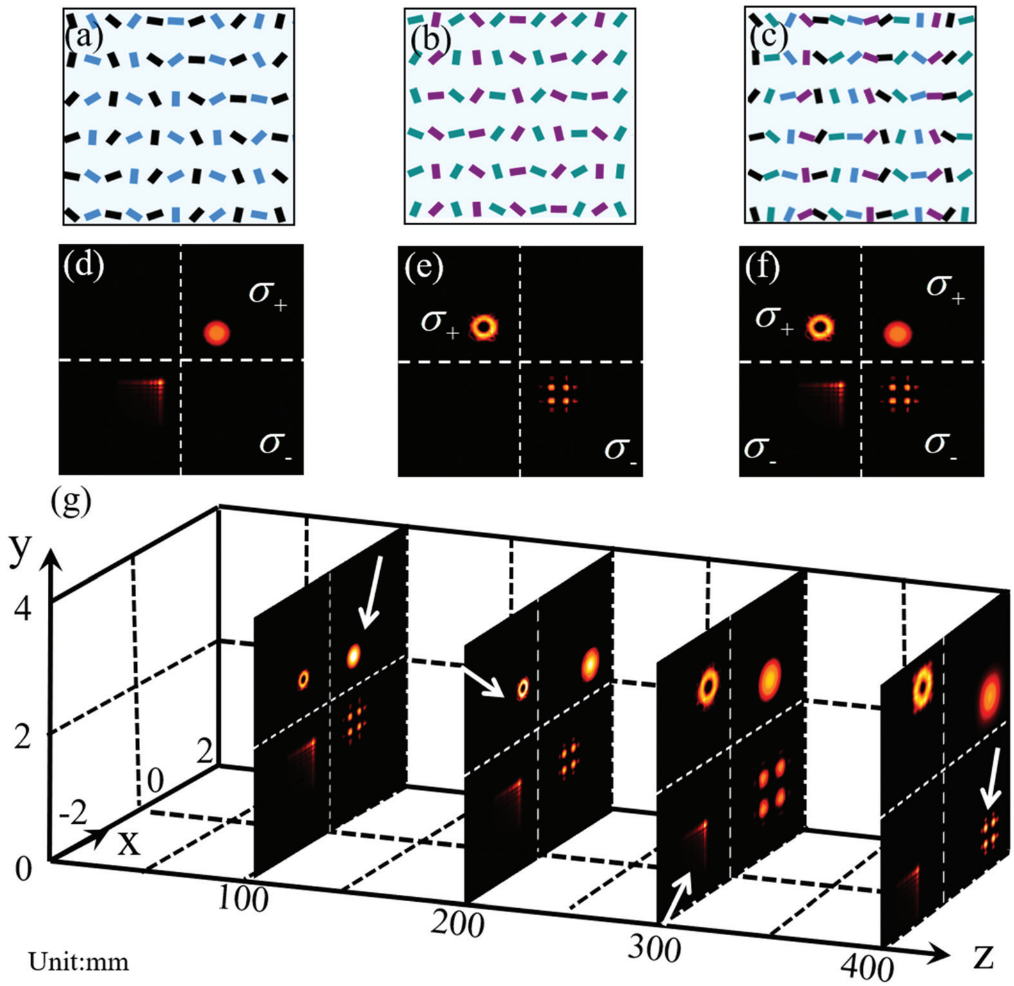

Fig. 5 Multifunctional spin-dependent metasurface demonstration. The first row is the axis orientation distribution of the metasurface. The second row is the calculated light field distribution after the propagation of 50 mm. The incident beam is a plane wave with normal incidence. (g) The spin-dependent beam evolution along the propagation direction. The focusing components are indicated with the white arrows at different focal planes.

Let us assume that the axis orientation in Fig. 5(a)–(c) is θ, which can be given as

$$\theta = \theta_a + \frac{2\pi}{\lambda}\frac{(x + k \times y)}{\Lambda_b} + \frac{2\pi}{\lambda}\sqrt{x^2 + y^2} + \frac{2\pi}{\lambda}\left(\sqrt{x^2 + y^2 + {f_c}^2} - f_c\right) \tag{1}$$

Here, θ_a = Arg(G) or Arg(A) is the phase of the Gaussian (Airy) beam; the parameter k is set for modulating the splitting direction of the spin components; and the period Λ_b is given by Λ_G = 0.14 mm for the Gaussian component and Λ_A = 0.25 mm for the Airy component. The last term is used for focusing the spin component at different positions. Here, f_c can be offered as f_G = 100 mm for the Gaussian component and f_A = 300 mm for the Airy component. The designed axis orientation distribution and the result of intensity distribution are displayed in Fig. 5(a) and (d). In Fig. 5(a), the black one is used for generating the left-handed Gaussian wavefront, while the blue one is for the Airy wavefront generation.

Using the same design approach for the vortex beam and Hermite beam, by setting the period of the grating as Λ_V = 0.22 mm, Λ_H = 0.45 mm, f_V = 200 mm, and f_H = 400 mm, the obtained results are shown in Fig. 5(b) and (e). In Fig. 5(b) the green one can be used for generating the left-handed vortex wavefront, while the purple one is for the Hermite wavefront generation. The combination result is shown in the last column. The corresponding axis orientation and intensity distribution are shown in Fig. 5(c) and (f). Fig. 5(g) demonstrates the intensity distribution of different spin components at the focal planes. As we know, in free space, the relationship between the propagating trajectory of the Airy wave packet ξ and the propagating distance z follows $\xi \propto z^2$.[38] As we can see, the square term depicts a parabolic trajectory as a function of distance z. Based on the phase gradient generated by our metasurface, for a fundamental Gaussian beam, it will be deflected with an angle $\pi x/\Lambda$, which modifies the previous Gaussian beam trajectory. Here, we can predict that the propagation of the Airy beam will first undergo deflection and then proceed along a parabolic trajectory, which will be away from its previous propagation direction and will be determined by our designed phase gradient.[39]

Discussion and conclusion

One of the significant parameters which can be employed to evaluate the performance of our metasurface is the diffraction efficiency, defined as $\eta = (P_{\mathrm{LCP}} + P_{\mathrm{RCP}})/(P_{\mathrm{LCP}} + P_{\mathrm{RCP}} + P_0)$, where P_{LCP}, P_{RCP} and P_0 are the output powers of the focused LCP, focused RCP and zero order components, respectively. The measured diffraction efficiencies obtained by using a Vega laser power meter (P/N: 7Z01560, OPHIR Photonics) in the experiment are approximately 45.2%, 48.5%, 48.4%, and 49.3% at wavelengths of 430 nm, 480 nm, 510 nm, and 633 nm, respectively. Here, the low diffraction efficiency is attributed to the existence of the defocused component, since in the diffraction efficiency equation, we only consider the focused component. The total transmission efficiencies by considering both focused and defocused components are 92.5%, 93.2%, 93.8%, and 94.2% at the four wavelengths mentioned above. The integrated metasurface presented in this work features the combination of several important functionalities and advantages, such as broadband, high efficiency, spatial multiplexing and compactness.[29] The concept of different spin components with unequal spin-dependent shift can also be employed to achieve the multichannel OAM, and the topological engineering of the OAM beam (see ESI Fig. S1†). The position of each OAM can be controlled, representing an additional degree of freedom for multi-photon entanglement.[40,41] Therefore, the capability to achieve multiple individual OAM beams and arbitrarily modulated OAM based on a single metasurface provides the possibility of highly compact devices in a quantum experimental system.[42] In addition, the focused chiral OAM component may generate a helical phase in the longitudinal component of the electric field, which makes particles trapping easier.[43]

In summary, we have demonstrated how a broadband metasurface can achieve spin controlled wavefront shaping for different spin components. In this work, by proper design of the mirror-symmetry violation, photonic spin-dependent splitting with different spin component types has been realized. In particular, we show how this composite metasurface can be used to transform a plane wave into a vortex beam and a Hermite beam with desired splitting angles depending on its polarization states. The proposed metasurface can be easily extended into more complex functionalities with the large-scale, high-resolution and low-cost method used in this work. The concept of a multifunctional spin-dependent composite (integrated and interleaved) metasurface may replace the bulky traditional lenses in existing optical systems and find potential applications in the fields of imaging, optical information processing, and optical communication.

Author contributions

H. L. and Z. L. developed the concept presented in this paper. J. Z. carried out the analytical and numerical modeling and designed the device. H. Q. conducted the measurement. H. L., Z. L. and S. W. supervised the entire project. J. Z. and H. Q. wrote the manuscript. All authors discussed the results and commented on the article.

Conflicts of interest

The authors declare no competing financial interest.

Acknowledgements

This work is supported by the National Natural Science Foundation of China (Grants no. 11474089) and the China Scholarship Council (scholarship 201606130065).

References

1 C. Ma and Z. Liu, A Super Resolution Metalens with Phase Compensation Mechanism, *Appl. Phys. Lett.*, 2010, **96**, 183103.
2 D. Lu and Z. Liu, Hyperlenses and Metalenses for Far-Field Super-Resolution Imaging, *Nat. Commun.*, 2012, **3**, 1205.
3 A. P. Mosk, A. Lagendijk, G. Lerosey and M. Fink, Controlling Waves in Space and Time for Imaging and Focusing in Complex Media, *Nat. Photonics*, 2012, **6**, 283–292.
4 Z. e. Bomzon, V. Kleiner and E. Hasman, Computer-Generated Space-Variant Polarization Elements with Subwavelength Metal Stripes, *Opt. Lett.*, 2001, **26**, 33–35.
5 N. Yu, P. Genevet, M. A. Kats, F. Aieta, J.-P. Tetienne, F. Capasso and Z. Gaburro, Light Propagation with Phase Discontinuities: Generalized Laws of Reflection and Refraction, *Science*, 2011, **334**, 333–337.
6 A. V. Kildishev, A. Boltasseva and V. M. Shalaev, Planar Photonics with Metasurfaces, *Science*, 2013, **339**, 1232009.
7 A. Pors, O. Albrektsen, I. P. Radko and S. I. Bozhevolnyi, Gap Plasmon-Based Metasurfaces for Total Control of Reflected Light, *Sci. Rep.*, 2013, **3**, 2155.
8 N. Yu and F. Capasso, Flat Optics with Designer Metasurfaces, *Nat. Mater.*, 2014, **13**, 139–150.
9 E. Hasman, V. Kleiner, G. Biener and A. Niv, Polarization Dependent Focusing Lens by Use of Quantized Pancharatnam–Berry Phase Diffractive Optics, *Appl. Phys. Lett.*, 2003, **82**, 328–330.
10 D. Fattal, J. Li, Z. Peng, M. Fiorentino and R. G. Beausoleil, Flat Dielectric Grating Reflectors with Focusing Abilities, *Nat. Photonics*, 2010, **4**, 466–470.
11 D. Lin, P. Fan, E. Hasman and M. L. Brongersma, Dielectric Gradient Metasurface Optical Elements, *Science*, 2014, **345**, 298–302.

12 K. E. Chong, I. Staude, A. James, J. Dominguez, S. Liu, S. Campione, G. S. Subramania, T. S. Luk, M. Decker and D. N. Neshev, Polarization-Independent Silicon Metadevices for Efficient Optical Wavefront Control, *Nano Lett.*, 2015, **15**, 5369–5374.

13 B. J. Bohn, M. Schnell, M. A. Kats, F. Aieta, R. Hillenbrand and F. Capasso, Near-Field Imaging of Phased Array Metasurfaces, *Nano Lett.*, 2015, **15**, 3851–3858.

14 J. Zhou, H. Qian, G. Hu, H. Luo, S. Wen and Z. Liu, Broadband Photonic Spin Hall Meta-Lens, *ACS Nano*, 2018, **12**, 82–88.

15 S. Ishii, A. V. Kildishev, V. M. Shalaev, K.-P. Chen and V. P. Drachev, Metal Nanoslit Lenses with Polarization-Selective Design, *Opt. Lett.*, 2011, **36**, 451–453.

16 A. Arbabi, Y. Horie, A. J. Ball, M. Bagheri and A. Faraon, Subwavelength-Thick Lenses with High Numerical Apertures and Large Efficiency Based on High-Contrast Transmitarrays, *Nat. Commun.*, 2015, **6**, 7069.

17 G. Hu, X. Hong, K. Wang, J. Wu, H.-X. Xu, W. Zhao, W. Liu, S. Zhang, F. Garcia-Vidal and B. Wang, Coherent Steering of Nonlinear Chiral Valley Photons with a Synthetic Au–Ws 2 Metasurface, *Nat. Photonics*, 2019, 1.

18 R. P. Chen, Z. Chen, Y. Gao, J. Ding and S. He, Flexible Manipulation of the Polarization Conversions in a Structured Vector Field in Free Space, *Laser Photonics Rev.*, 2017, **11**, 1700165.

19 P. C. Wu, W. Zhu, Z. X. Shen, P. H. J. Chong, W. Ser, D. P. Tsai and A. Q. Liu, Broadband Wide-Angle Multifunctional Polarization Converter Via Liquid-Metal-Based Metasurface, *Adv. Opt. Mater.*, 2017, **5**, 1600938.

20 J. Kim, S. Choudhury, C. DeVault, Y. Zhao, A. V. Kildishev, V. M. Shalaev, A. Alù and A. Boltasseva, *Controlling the Polarization State of Light with Plasmonic Metal Oxide Metasurface*, 2016.

21 X. Ni, N. K. Emani, A. V. Kildishev, A. Boltasseva and V. M. Shalaev, Broadband Light Bending with Plasmonic Nanoantennas, *Science*, 2012, **335**, 427–427.

22 M. Khorasaninejad, W. T. Chen, R. C. Devlin, J. Oh, A. Y. Zhu and F. Capasso, Metalenses at Visible Wavelengths: Diffraction-Limited Focusing and Subwavelength Resolution Imaging, *Science*, 2016, **352**, 1190–1194.

23 M. Khorasaninejad, A. Y. Zhu, C. Roques-Carmes, W. T. Chen, J. Oh, I. Mishra, R. C. Devlin and F. Capasso, Polarization-Insensitive Metalenses at Visible Wavelengths, *Nano Lett.*, 2016, **16**, 7229–7234.

24 D. Wen, F. Yue, G. Li, G. Zheng, K. Chan, S. Chen, M. Chen, K. F. Li, P. W. H. Wong and K. W. Cheah, Helicity Multiplexed Broadband Metasurface Holograms, *Nat. Commun.*, 2015, **6**, 8241.

25 Y. Guo, M. Pu, Z. Zhao, Y. Wang, J. Jin, P. Gao, X. Li, X. Ma and X. Luo, Merging Geometric Phase and Plasmon Retardation Phase in Continuously Shaped Metasurfaces for Arbitrary Orbital Angular Momentum Generation, *ACS Photonics*, 2016, **3**, 2022–2029.

26 J. B. Mueller, N. A. Rubin, R. C. Devlin, B. Groever and F. Capasso, Metasurface Polarization Optics: Independent Phase Control of Arbitrary Orthogonal States of Polarization, *Phys. Rev. Lett.*, 2017, **118**, 113901.

27 F. Zhang, M. Pu, X. Li, P. Gao, X. Ma, J. Luo, H. Yu and X. Luo, All-Dielectric Metasurfaces for Simultaneous Giant Circular Asymmetric Transmission and Wavefront Shaping Based on Asymmetric Photonic Spin–Orbit Interactions, *Adv. Funct. Mater.*, 2017, **27**, 1704295.

28 E. Maguid, I. Yulevich, D. Veksler, V. Kleiner, M. L. Brongersma and E. Hasman, Photonic Spin-Controlled Multifunctional Shared-Aperture Antenna Array, *Science*, 2016, aaf3417.

29 S. Kruk, F. Ferreira, N. Mac-Suibhne, C. Tsekrekos, I. Kravchenko, A. Ellis, D. Neshev, S. Turitsyn and Y. Kivshar, Transparent Dielectric Metasurfaces for Mode Modulation and Spatial Multiplexing, 2017, *arXiv preprint arXiv*:1711.07160.

30 Z. e. Bomzon, G. Biener, V. Kleiner and E. Hasman, Space-Variant Pancharatnam–Berry Phase Optical Elements with Computer-Generated Subwavelength Gratings, *Opt. Lett.*, 2002, **27**, 1141–1143.

31 S. Pancharatnam, Generalized Theory of Interference, and Its Applications, in *Proceedings of the Indian Academy of Sciences-Section A*, Springer, 1956, pp. 247–262.

32 M. V. Berry, Quantal Phase Factors Accompanying Adiabatic Changes, in *Proceedings of the Royal Society of London A: Mathematical, Physical and Engineering Sciences*, The Royal Society, 1984, pp. 45–57.

33 A. E. Siegman and S. Lasers, *California*, University Science Books, 1986, vol. 586, pp. 589.

34 M. Beresna, M. Gecevičius, P. G. Kazansky and T. Gertus, Radially Polarized Optical Vortex Converter Created by Femtosecond Laser Nanostructuring of Glass, *Appl. Phys. Lett.*, 2011, **98**, 201101.

35 L. Marrucci, C. Manzo and D. Paparo, Optical Spin-to-Orbital Angular Momentum Conversion in Inhomogeneous Anisotropic Media, *Phys. Rev. Lett.*, 2006, **96**, 163905.

36 Y. Shimotsuma, P. G. Kazansky, J. Qiu and K. Hirao, Self-Organized Nanogratings in Glass Irradiated by Ultrashort Light Pulses, *Phys. Rev. Lett.*, 2003, **91**, 247405.

37 D. Hakobyan and E. Brasselet, Left-Handed Optical Radiation Torque, *Nat. Photonics*, 2014, **8**, 610–614.

38 G. Siviloglou, J. Broky, A. Dogariu and D. Christodoulides, Observation of Accelerating Airy Beams, *Phys. Rev. Lett.*, 2007, **99**, 213901.

39 P. Zhang, S. Wang, Y. Liu, X. Yin, C. Lu, Z. Chen and X. Zhang, Plasmonic Airy Beams with Dynamically Controlled Trajectories, *Opt. Lett.*, 2011, **36**, 3191–3193.

40 B. Jack, A. Yao, J. Leach, J. Romero, S. Franke-Arnold, D. Ireland, S. Barnett and M. Padgett, Entanglement of Arbitrary Superpositions of Modes within Two-Dimensional Orbital Angular Momentum State Spaces, *Phys. Rev. A*, 2010, **81**, 043844.

41 B. Hiesmayr, M. de Dood and W. Löffler, Observation of Four-Photon Orbital Angular Momentum Entanglement, *Phys. Rev. Lett.*, 2016, **116**, 073601.

42 T. Lei, M. Zhang, Y. Li, P. Jia, G. N. Liu, X. Xu, Z. Li, C. Min, J. Lin and C. Yu, Massive Individual Orbital Angular Momentum Channels for Multiplexing Enabled by Dammann Gratings, *Light: Sci. Appl.*, 2015, **4**, e257.

43 Y. Zhao, J. S. Edgar, G. D. Jeffries, D. McGloin and D. T. Chiu, Spin-to-Orbital Angular Momentum Conversion in a Strongly Focused Optical Beam, *Phys. Rev. Lett.*, 2007, **99**, 073901.